

WHAT IS THE PHYSICAL ORIGIN OF STRONG Ly α EMISSION? I. DEMOGRAPHICS OF Ly α EMITTER STRUCTURES*

TAKATOSHI SHIBUYA^{1,2}, MASAMI OUCHI^{1,3}, KIMIHIKO NAKAJIMA^{3,4}, SURAPHONG YUMA¹,
 TAKUYA HASHIMOTO³, KAZUHIRO SHIMASAKU^{3,5}, MASAO MORI², AND MASAYUKI UMEMURA²

¹ Institute for Cosmic Ray Research, The University of Tokyo, 5-1-5 Kashiwanoha,

Kashiwa, Chiba 277-8582, Japan; shibuyat_k_at_icrr.u-tokyo.ac.jp

² Center for Computational Sciences, The University of Tsukuba, 1-1-1 Tennodai, Tsukuba, Ibaraki 305-8577 Japan

³ Department of Astronomy, Graduate School of Science, The University of Tokyo, Tokyo 113-0033, Japan

⁴ Institute for the Physics and Mathematics of the Universe (IPMU), TODIAS, The University of Tokyo,
 5-1-5 Kashiwanoha, Kashiwa, Chiba 277-8583, Japan

⁵ Research Center for the Early Universe, Graduate School of Science, The University of Tokyo, Tokyo 113-0033, Japan

Received 2013 December 27; accepted 2014 February 21; published 2014 March 26

ABSTRACT

We present the results of structure analyses for a large sample of 426 Ly α emitters (LAEs) at $z \sim 2.2$ that are observed with the *Hubble Space Telescope*/Advanced Camera for Surveys and WFC3-IR during deep extra-galactic legacy surveys. We confirm that the merger fraction and the average ellipticity of LAE's stellar component are 10%–30% and 0.4–0.6, respectively, that are comparable with previous study results. We successfully identify that some LAEs have a spatial offset between Ly α and stellar-continuum emission peaks, $\delta_{\text{Ly}\alpha}$, by ~ 2.5 –4 kpc beyond our statistical errors. To uncover the physical origin of strong Ly α emission found in LAEs, we investigate the Ly α equivalent width (EW) dependences of three structural parameters: merger fraction, $\delta_{\text{Ly}\alpha}$, and ellipticity of stellar distribution in the range of $\text{EW}(\text{Ly}\alpha) = 20$ –250 Å. Contrary to expectations, we find that the merger fraction does not significantly increase with Ly α EW. We reveal an anti-correlation between $\delta_{\text{Ly}\alpha}$ and $\text{EW}(\text{Ly}\alpha)$ using a Kolmogorov–Smirnov (K-S) test. There is a trend that the LAEs with a large Ly α EW have a small ellipticity. This is consistent with the recent theoretical claims that Ly α photons can more easily escape from face-on disks having a small ellipticity, due to less inter-stellar gas along the line of sight, although our K-S test indicates that this trend is not statistically significant. Our results of Ly α -EW dependence generally support the idea that an H I column density is a key quantity determining Ly α emissivity.

Key words: cosmology: observations – early universe – galaxies: formation – galaxies: high-redshift

Online-only material: color figures

1. INTRODUCTION

Ly α Emitters (LAEs) are a population of high- z star-forming galaxies selected with narrow-band (NB) and broad-band (BB) filters to identify their prominent Ly α emission. A large number of NB observations have been carried out to study LAEs at $z \sim 3$ –7 and beyond $z = 7$ (e.g., Cowie et al. 2010; Gronwall et al. 2007; Ciardullo et al. 2012; Ouchi et al. 2008, 2010; Hu et al. 2010; Finkelstein et al. 2007; Kashikawa et al. 2011, 2006; Shibuya et al. 2012; Ota et al. 2008). Based on high resolution imaging and spectral energy distribution (SED) fitting, such a galaxy population is thought to be typically young, compact, less-massive, less-dusty, and a possible progenitor of Milky Way mass galaxies (e.g., Gronwall et al. 2011; Guaita et al. 2011; Ono et al. 2010; Gawiser et al. 2007; Dressler et al. 2011; Rauch et al. 2008). LAEs are also used as a powerful probe to estimate the neutral hydrogen fraction at the reionizing epoch, because Ly α photons are absorbed by the intergalactic medium.

Despite the significant importance of LAEs in galaxy formation and cosmology, the Ly α emitting mechanism is not completely understood due to the highly complex resonant nature of Ly α in the interstellar medium (ISM). Many theoretical models have predicted that the neutral gas and/or dust distributions surrounding central ionizing sources are closely related to the escape of Ly α (e.g., Laursen et al. 2013, 2009; Laursen & Sommer-Larsen 2007; Duval et al. 2014; Zheng & Wallace 2013; Zheng

et al. 2010; Yajima et al. 2012a). Resonant scattering in the neutral ISM results in a significant attenuation of Ly α . The Ly α absorbing ISM may be blown out by galaxy mergers and subsequent galactic outflows. The galactic interactions would also trigger star formation and enhance the Ly α emissivity. In fact, merging features have been found in the LAE population in several observational studies (e.g., Bond et al. 2009, 2010, 2012; Gronwall et al. 2011). These studies have investigated various morphological properties for ~ 100 –200 LAEs at $z \sim 2$ –3, but have not examined dependences on Ly α emissivity.

It is also informative to investigate Ly α emitting positions relative to star forming regions. The geometry of the surrounding neutral gas might leave an imprint on the spatial offsets between Ly α and stellar-continuum emission. Jiang et al. (2013) have investigated the spatial offsets for ~ 70 LAEs at $z = 6$ –7 and found misalignments in several objects. However, they have not studied systematically the spatial offsets and their dependence on the physical properties of LAEs.

In addition, the galactic morphologies are considered to be relevant to the Ly α emissivity. Copious amounts of gas and/or dust are likely to inhabit the galactic disk. Consequently, Ly α photons preferentially escape perpendicular to the disk. The inclination effect on Ly α emissivity has been widely examined theoretically (e.g., Zheng & Wallace 2013; Verhamme et al. 2012; Charlot & Fall 1993; Chen & Neufeld 1994; Barnes et al. 2011; Laursen & Sommer-Larsen 2007; Laursen et al. 2009; Zheng et al. 2010). These studies have predicted the preferential escape of Ly α in the face-on direction.

* Based on data obtained with the Subaru Telescope operated by the National Astronomical Observatory of Japan.

However, these structural properties and their dependences on Ly α emissivity have not yet been examined statistically for high- z LAEs. Ly α emissivity is closely related to Ly α equivalent width (EW), since the EW represents a Ly α luminosity normalized by star formation activity in a galaxy. A systematic study of the relation between the structures of LAEs and their Ly α EW will provide crucial hints concerning the neutral gas distributions and associated Ly α emitting mechanisms.

This is the first paper in a series exploring the Ly α emitting mechanisms.⁶ In this paper, we present the results of our study on the structures of $z \sim 2.2$ LAEs to verify the Ly α -EW dependence of the merger fraction, Ly α spatial offset $\delta_{\text{Ly}\alpha}$, and ellipticity by exploiting the *Hubble Space Telescope* (*HST*)/Advanced Camera for Surveys (ACS) and Wide Fields Camera 3 (WFC3) images. We use our statistically large sample consisting of ~ 3400 LAEs constructed with Subaru NB observations. First, we describe the details of our $z = 2.2$ LAE sample for our structure analyses in Section 2. Next, we explain the methods we use to derive structural quantities in the rest-frame UV/optical emission in Section 3. We examine the dependence of the derived morphological quantities on Ly α EW in Section 4. In Section 5, we discuss the physical mechanisms by which high- z galaxies emit Ly α . In Section 6, we summarize our findings.

Throughout this paper, we adopt the concordance cosmology with $(\Omega_m, \Omega_\Lambda, h) = (0.3, 0.7, 0.7)$ (Komatsu et al. 2011). All magnitudes are given in the AB system (Oke & Gunn 1983).

2. SAMPLE

Our LAE sample for the structure analysis has been constructed using observations from Subaru/Suprime-Cam (Miyazaki et al. 2002) equipped with the NB filter, NB387 ($\lambda_c = 3870 \text{ \AA}$ and FWHM = 94 \AA ; Nakajima et al. 2012). The Suprime-Cam observations were carried out for LAEs at $z = 2.2$ with NB387 in a total area of $\sim 1.5 \text{ deg}^2$. Based on the color selection of $B - \text{NB387}$ and $u^* - \text{NB387}$, the Suprime-Cam observations located 619, 919, 747, 950, and 168 LAEs in the Cosmic Evolution Survey (COSMOS; Scoville et al. 2007), the Subaru/XMM-Newton Deep Survey (SXDS; Furusawa et al. 2008), the Chandra Deep Field South (Giacconi et al. 2001), the *Hubble* Deep Field North (Giavalisco et al. 2004), and the SSA22 (e.g., Steidel et al. 2000) fields, respectively. In the above five fields, a total of ~ 3400 LAEs have been selected down to a Ly α EW of 20–30 \AA in rest-frame (K. Nakajima et al., in preparation). This large sample size enables us to study statistically various properties of high- z LAEs, such as their metal abundances (Nakajima et al. 2012, 2013), Ly α velocity offset (Hashimoto et al. 2013; Shibuya et al. 2014), and Ly α halo (R. Momose et al., in preparation). Details of observations and selection for LAEs are presented in Nakajima et al. (2012, 2013).

3. METHODOLOGY

In this section, we describe the methods of our structure analysis using the *HST* data. We focus mainly on three structural properties: the merger fraction (Section 3.2), the spatial offset between Ly α and stellar-continuum positions $\delta_{\text{Ly}\alpha}$ (Section 3.3), and the ellipticity (Section 3.4).

We use the I_{814} and H_{160} data taken with ACS and WFC3 on *HST*, respectively, to examine the rest-frame UV and optical morphology of the LAE counterparts. The COSMOS, SXDS,

Table 1
Number of Our Ly α Emitters

Field (1)	m_{lim} (2)	Number of LAEs (3)
<i>I</i> ₈₁₄ on ACS		
COSMOS-Wide	27.0	564
CANDELS GOODS-S	28.5	213
CANDELS GOODS-N	28.3	95
CANDELS UDS	28.4	70
Total number		942
<i>H</i> ₁₆₀ on WFC3		
CANDELS COSMOS	26.9	86
CANDELS GOODS-S	26.7–27.6	65
CANDELS GOODS-N	26.5	63
CANDELS UDS	27.1	83
Total number		297

Notes. Columns: (1) Field. (2) 5σ limiting magnitude in a $0''.2$ aperture. (3) Number of $z = 2.2$ LAEs taken with *HST*.

and GOODS-North and South fields are partially imaged by the Cosmic Assembly Near-infrared Deep Extragalactic Legacy Survey (CANDELS; Grogin et al. 2011; Koekemoer et al. 2011) with *HST*/ACS and WFC3. The 5σ limiting magnitudes in a $0''.2$ aperture are 28.3–29.4 in I_{814} and 26.5–27.6 in H_{160} . Additionally, the COSMOS field is mostly covered by the ACS imaging with the I_{814} filter (COSMOS-Wide; Koekemoer et al. 2007; Massey et al. 2010); however, its depth is ~ 1 –2 mag shallower than that of CANDELS. We use both the CANDELS and COSMOS-Wide fields for our morphological analysis. The typical sizes of the point spread function (PSF) are $0''.09$ and $0''.18$ (~ 0.75 and ~ 1.5 kpc at $z = 2.2$) in the I_{814} and H_{160} images, respectively. The number of LAEs in the *HST* fields are summarized in Table 1.

3.1. Identifications of LAE Counterparts

In order to search for UV and optical counterparts of our LAEs, we first extract $3'' \times 3''$ cutout images from the I_{814} and H_{160} data at the position of each LAE in a manner similar to previous morphological studies (Bond et al. 2009, 2010, 2012; Gronwall et al. 2011). The size of the cutouts is exactly the same as in Bond et al. (2012), who have studied the morphology of $z = 2.1$ LAEs. In total, we obtain 942 and 297 cutout images of the I_{814} and H_{160} bands, respectively.

Next, we detect sources in the *HST* cutout images and perform photometry for all of the sources having an area larger than five contiguous pixels (DETECT_MINAREA = 5) with a flux greater than 2.5σ over the sky surface brightness (DETECT_THRESH = 2.5) using SExtractor version 2.8.6 (Bertin & Arnouts 1996). Our DETECT_THRESH value is higher than that in Bond et al. (2012, ; DETECT_THRESH = 1.65). Because one of our aims is to estimate the merger fraction from the number of close galaxy pairs (Section 3.2.1), a reliable detection of objects is required even for very faint sources. If a low DETECT_THRESH value is chosen, then false detections increase, leading to an overestimate of the merger fraction. Here, we tune a DETECT_THRESH parameter to identify real galaxy pairs by visual inspection. Meanwhile, DETECT_THRESH is set to 1.65 instead of 2.5 when we derive the morphological indices for counterparts of LAEs in Section 3.2.2.

Finally, we define the I_{814} and H_{160} counterparts of LAEs as objects within a radius of $0''.65$ (~ 5.4 kpc at $z = 2.2$) from an

⁶ The second paper presents a kinematic study for LAEs (Shibuya et al. 2014).

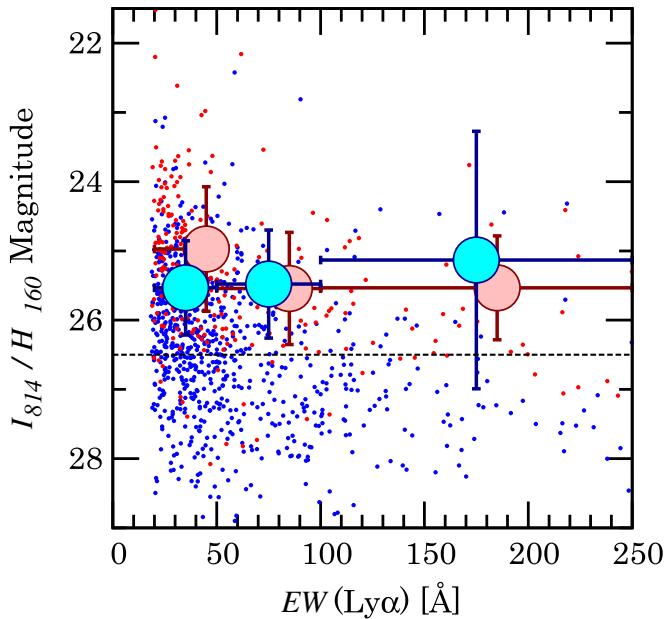


Figure 1. Ly α EW and I_{814}/H_{160} magnitudes of continuum counterparts. The blue and red dots denote counterparts in I_{814} and H_{160} data, respectively. The large cyan and magenta circles are the average I_{814} and H_{160} magnitudes, respectively, in EW bins of 20–50, 50–100, and >100 Å. The large magenta circles are slightly shifted along x -axis for the sake of clarity. The dashed horizontal line represents the magnitude cut for the close-pair method, $m = 26.5$. With the magnitude cut, the average continuum magnitudes of EW bins are comparable between the EW bins.

(A color version of this figure is available in the online journal.)

NB source center, following the definition of Bond et al. (2012). According to the assessment by Bond et al. (2012), this selection radius can effectively exclude field sources. Figure 1 shows the Ly α EW and I_{814}/H_{160} magnitudes of the counterparts. Figure 1 reproduces the Ando effect (Ando et al. 2006) that Ly α EW anticorrelates with continuum magnitudes. We adopt a continuum magnitude cut of 26.5 mag, and derive the average I_{814}/H_{160} magnitudes in each Ly α EW bin of 20–50, 50–100, and >100 Å. These average values are almost constant within a 1σ error bar between the EW bins. In our analyses, we only use objects with a continuum brighter than 26.5 mag.

3.2. Merger Fraction

We estimate the merger fraction of our LAE sample using two methods, the close-pair method (Section 3.2.1) and the morphological index method (Section 3.2.2). The former is used to count the number of resolved sources falling within a specific selection radius. The latter is used to classify mergers with the non-parametric morphological indices, *CAS* (Conselice et al. 2000; Conselice 2003), for the sources that are unresolved in the close-pair method. In a merger process, galaxies first approach each other, and then undergo coalescence(s). The close-pair method selects merger objects in the approaching phase, and the index method identifies the final coalescence phase. In calculations of morphological indices, all of the sources in a selection radius are usually considered to be a galaxy system, even if they are clearly isolated. Using the morphological indices, we aim to examine whether unresolved single sources are interacting (correspondingly morphologically disturbed) galaxies or intrinsically isolated components. The classification with the morphological indices is complementary to the close-pair method which identifies mergers with discrete components.

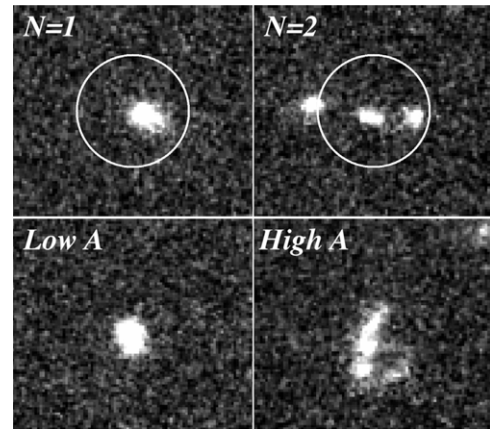


Figure 2. Example I_{814} images of mergers and non-mergers in the close-pair (top panels) and the morphological index methods (bottom panels). The UV counterparts in the top left and right panels show single and multiple components, respectively, within our selection radius of $0''.65$ (white circles). The latter object is classified as a merger in the close-pair method. The UV counterparts in the bottom left and right panels have a low and high value of asymmetry, respectively. The object with a high A represents a highly disturbed structure. North is up and east is to the left.

3.2.1. Close-pair Method

The close-pair method has been used to identify mergers at low- (e.g., Ellison et al. 2013; Le Fèvre et al. 2000) and high- z (e.g., Law et al. 2012b). It is extremely difficult to detect the faint components of minor mergers at high- z . In our analysis, we consider only major mergers with multiple components of comparable flux (a flux ratio of 0.3–1). By counting the number of sources within the selection radius, $r_{\text{sel}} = 0''.65$ (Section 3.1), we simply define (major) mergers as counterparts with multiple sources. Figure 2 shows representative examples of a merger and a non-merger classified with the close-pair method.

We carry out Monte Carlo simulations with artificial galaxy pairs to estimate the detection completeness of major mergers. We consider two cases of flux ratios in major merger components, 0.3–1 and 0.5–1. We create 100 galaxy pairs with GALLIST and MKOBJECTS in the IRAF package in bins of I_{814}/H_{160} magnitudes. In this procedure, we make these artificial galaxies at a redshift and do not take into account the distance along the line of sight between components. This is because we aim to simply estimate the detection completeness of the fainter component as a function of *HST*-band magnitudes. On the other hand, our selection radius efficiently finds intrinsically interacting objects, minimizing the chance projection rate of $\sim 10\%$ (see Bond et al. 2012). The created galaxy pairs are embedded into cutout images of randomly selected blank fields. We detect these pairs in the same manner as for LAEs.

The estimated completeness is shown in Figure 3. The artificial merger events with a flux ratio of 0.5–1 are reproduced well for pairs brighter than 26.5 mag in I_{814} ($>50\%$). The completeness in H_{160} is approximately half of that in I_{814} at 26.0–26.5 mag. This leads to the difference of derived merger fractions in I_{814} and H_{160} in Section 4.1. In the case of the mergers with a flux ratio of 0.3–1, the completeness is only $\sim 50\%$ even at <24 mag in I_{814}/H_{160} . This is because the magnitudes are severely underestimated for fainter components in the 0.3:1 merger.

As a result, we use 426 and 237 LAEs brighter than 26.5 mag in I_{814} and H_{160} , respectively, in the close-pair method. Table 2 summarizes the numbers of the LAEs used, including those in

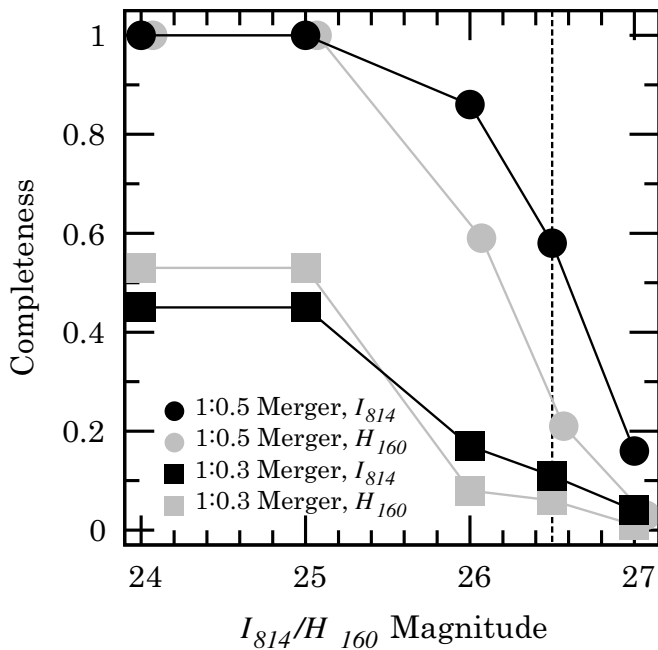


Figure 3. Completeness of merger identification as a function of I_{814} (black lines) and H_{160} (gray lines) magnitudes. The filled circles and squares denote the completeness with the component's flux ratios of 0.5–1 and 0.3–1, respectively. The dashed vertical line is a magnitude cut of 26.5 mag for the close-pair method. The gray circles are slightly shifted along x-axis for the sake of clarity.

the following analyses. We provide the derived merger fraction and its dependence on Ly α EW in Section 4.1.

3.2.2. Morphological Index Method

The non-parametric morphological indices have been widely utilized to characterize the structure and morphology of nearby and high- z galaxies (e.g., Cassata et al. 2007; Zamojski et al. 2007; Scarlata et al. 2007).

The CAS system consists of the concentration (C), asymmetry (A), and smoothness (S) proposed by Abraham et al. (1996), Conselice et al. (2000), and Conselice (2003). Concentration C is an index representing how much the flux concentrates in the galaxy's center. We calculate C using the definition of Conselice (2003), $C = 5 \log(r_{80}/r_{20})$, where r_{80} and r_{20} are the radii which contain 80% and 20% of the total flux of the galaxy, respectively. Asymmetry A quantifies the degree of the rotational symmetry of the galaxy's light profile. It is calculated by

$$A \equiv A_{\text{obj}} - A_{\text{sky}} = \frac{\sum |F - F_{180}|}{\sum |F|} - \frac{\sum |B - B_{180}|}{\sum |B|}, \quad (1)$$

where F and F_{180} (B and B_{180}) are the original image of the galaxy (sky background) and its image rotated by 180° around the galaxy's center, respectively. The value of A ranges from zero to one. Asymmetry becomes zero for a galaxy with a completely rotationally symmetric light profile. The first term in the definition of A is the asymmetry of a galaxy. The second term is the apparent asymmetry caused by the sky background. We use average values of A_{sky} as representative of A_{sky} in each field (e.g., Scarlata et al. 2007). Both A_{obj} and A_{sky} are computed by using all pixels contained within a 1.5 Petrosian radius of a targeted galaxy (Petrosian 1976). The rotational center is defined as the position minimizing A in the 3×3 grid searching method (Conselice et al. 2000). The determined rotational center is also applied to the calculation of C . Since smoothness S cannot

Table 2
Number of Our Ly α Emitters for Each Analysis

Quantity (1)	Criteria (2)	Number of LAEs (3)
Merger fraction	$(I_{814} < 26.5)$	426
	$(H_{160} < 26.5)$	237
Ly α spatial offset	$(\text{NB387} < 24.5 \ \& \ I_{814} < 26.5)$	106
	$(\text{NB387} < 24.5 \ \& \ H_{160} < 26.5)$	40
Ellipticity	$(I_{814} < 25.0 \ \& \ R_e > 0''.09)$	41
	$(H_{160} < 25.0 \ \& \ R_e > 0''.18)$	35

Notes. Columns: (1) Quantity. (2) Magnitude and size cuts applied in each investigation. (3) Number of LAEs.

be correctly calculated for high- z galaxies (Lotz et al. 2004; Conselice & Arnold 2009), we do not use S in our analysis.

To check the adequacy of our calculation, we compute CA for other galaxies whose morphological indices have already been derived in previous studies. Cassata et al. (2007) calculated the indices for $\sim 23,000$ galaxies at low- z in the COSMOS-Wide field. From their sample, we extract 300 galaxies whose I_{814} magnitudes are comparable to those of our LAEs and calculate their CA . Our calculation reproduces well the results of Cassata et al. (2007). We apply the 1σ standard deviation from the CA values obtained in Cassata et al. (2007) to the errors of the derived indices for our LAE sample.

The morphological indices cannot be robustly calculated for objects with a low signal-to-noise ratio (e.g., Cassata et al. 2007). To obtain reliable values of the indices, we use LAEs with I_{814} and H_{160} magnitudes brighter than 25.0 mag in our CA calculation. The magnitude cut of 25.0 mag has usually been applied in previous morphological studies with *HST* data (e.g., Cassata et al. 2007). We also exclude objects whose half light radii in I_{814} and H_{160} are smaller than $0''.09$ and $0''.18$, which are unresolved with ACS and WFC3, respectively. We use 41 in I_{814} and 35 LAEs in H_{160} , respectively, that meet all of these selection criteria. Representative examples of objects with high and low A values are shown in Figure 2. The calculated morphological indices of our LAE sample are shown in Figure 4. The distributions of indices in these parameter spaces are quite similar to the results of Lyman break galaxies (LBGs) at $z \sim 2$ –3 (e.g., Law et al. 2012b).

In order to classify mergers, we adopt the following criterion,

$$A > 0.30, \quad (2)$$

which is defined by Lotz et al. (2008) for high- z galaxies. We do not use the C parameter for the merger classification, but we make the C – A diagram simply for the sake of clarity (Figure 4).

In the A classification, we identify mergers that are brighter than a specific MAG_APER magnitude (MAG_APER cut) in addition to the MAG_AUTO cut. The MAG_AUTO cut mistakenly selects objects with extremely low surface brightness. The asymmetry parameter might be overestimated for these objects due to their diffuse structure. We also derive the merger fraction for the sample selected in the MAG_APER cut to eliminate the diffuse objects. We use a $0''.3$ aperture to calculate MAG_APER. The number of selected counterparts significantly decreases, especially in the H_{160} data. Even in this case, we find a similar trend of Ly α EW dependence as in the MAG_AUTO cut.

We discuss the merger fraction based on the index classification in Section 4.1.

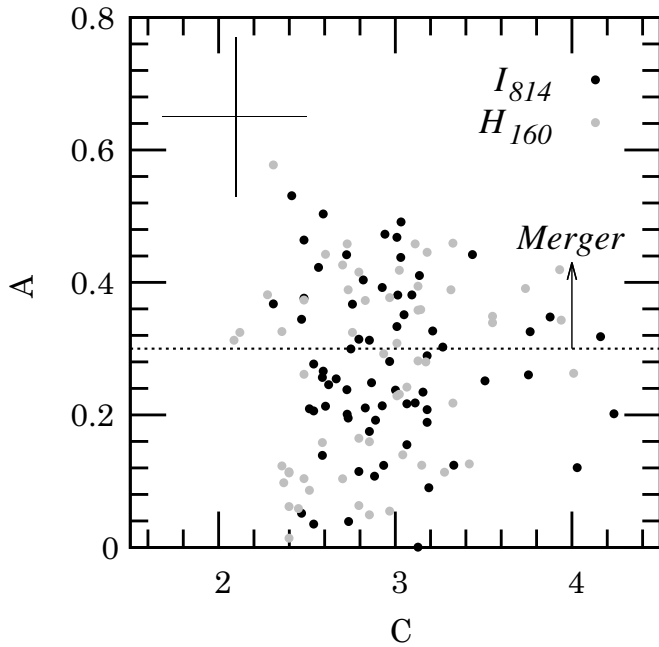


Figure 4. Concentration (C) and asymmetry (A) for counterparts in I_{814} (black circles) and H_{160} (gray circles). The region above the dashed line ($A = 0.30$) indicates the merger regime. The error bar in the upper corner represents the typical uncertainty in individual objects.

3.3. $\text{Ly}\alpha$ Spatial Offset Between Rest-frame UV/Optical Continuum and $\text{Ly}\alpha$ Emission

We calculate the projected distance between the rest-frame UV/optical continuum positions and the centroids of $\text{Ly}\alpha$ emission. In this calculation, we consider two types of components in stellar-continuum emission. One type is the brightest components in all of the sources within the selection radius, and the other type is the nearest ones from $\text{Ly}\alpha$ centroids among objects identified in our detection criteria of SExtractor (the top panel of Figure 5). The central position of each *HST* cutout image corresponds to $\text{Ly}\alpha$ centroids. We calculate $\delta_{\text{Ly}\alpha}$ from the coordinates of sources in the cutout images.

We find that the $\text{Ly}\alpha$ centroids are slightly shifted in toward the extended and diffuse light structure in several NB images, as shown in the top panel of Figure 5. The central position of LAEs has been determined by performing source detection with SExtractor in whole $\sim 30' \times 30'$ Suprime-Cam images (Nakajima et al. 2012; the magenta cross). The small positional offsets of $\text{Ly}\alpha$ are certainly caused by setting DETECT_THRESH to a relatively low value (2.0σ) for the LAE selection in the wide images. They have used a typical value of DETECT_THRESH in selections for high- z galaxies. That value is too low to estimate the peak position of $\text{Ly}\alpha$.

In order to estimate the peak position of $\text{Ly}\alpha$, we carry out the source detection with a higher DETECT_THRESH value (2.5σ) in each NB cutout image than the value used in the NB selection. This procedure is very efficient for calculating the $\text{Ly}\alpha$ spatial offset from the position where $\text{Ly}\alpha$ is emitted most efficiently. This position corresponds to the location where the galaxy is brightest in $\text{Ly}\alpha$. In the re-detection process, NB centroids are slightly shifted for several objects and we obtain redefined values of $\delta_{\text{Ly}\alpha}$. We adopt the original centroids for objects with a $\text{Ly}\alpha$ positional difference smaller than $0''.1$ corresponding to ~ 0.5 pixel in NB images.

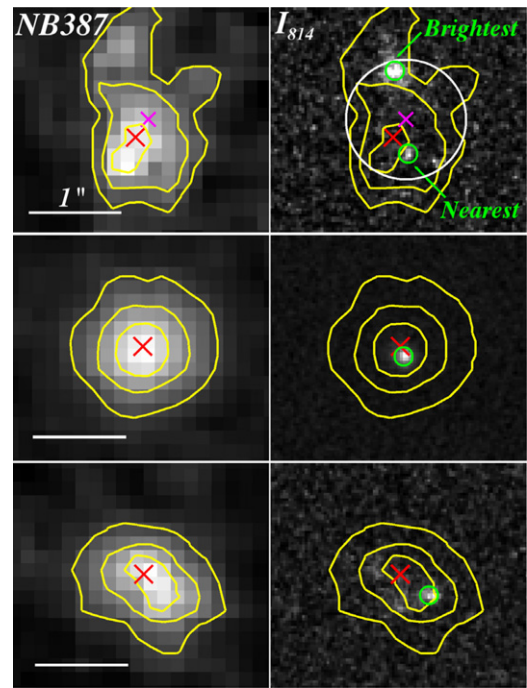


Figure 5. NB387 (left) and I_{814} (right) images of three example LAEs. The yellow contours indicate the isophotal area in the NB387 images. The green open circles denote the continuum counterparts in each I_{814} image. Top: LAE whose NB centroid is redefined. The magenta crosses depict the original position determined in the NB387 imaging studies (Nakajima et al. 2012, 2013). The red crosses represent the central position redefined from the SExtractor detection with a higher DETECT_THRESH value in the NB387 images. The NB centroid shifts by $\sim 0''.2$ toward the peak of light profile. See Section 3.3. The top and bottom green circles are the brightest and nearest continuum counterparts, respectively. The spatial offsets from the redefined NB center are $\sim 0''.7$ for the brightest and $\sim 0''.2$ for the nearest counterpart. The white circle indicates our selection radius of $0''.65$. Middle: LAE whose $\text{Ly}\alpha$ centroids are aligned well on the position of continuum emission. Bottom: LAE having a large $\delta_{\text{Ly}\alpha}$. The $\text{Ly}\alpha$ EW (the $\text{Ly}\alpha$ spatial offset) of the object in the middle and bottom panels are 218 ($0''.11$) and 38 Å ($0''.40$), respectively. The white bars in the lower corner of each NB387 image indicate $1''$, corresponding to ~ 8.3 kpc at $z = 2.2$. North is up and east is to the left.

(A color version of this figure is available in the online journal.)

We create artificial galaxies to estimate positional errors using the same method as described in Section 3.2.1. Figures 6 and 7 show the estimated positional errors of the I_{814}/H_{160} and NB387 images, respectively. These figures indicate that the positional uncertainties tend to be larger for fainter objects. In the *HST* images, the positional error is less than $\sim \pm 0''.02$ at I_{814}/H_{160} magnitudes brighter than 26.5. In contrast, the NB387 images have a large positional error of $\sim 0''.3$ (at 1σ) even at NB387 = 24.5. This large uncertainty is due to the relatively large seeing sizes ($\sim 0''.8$) in the NB data obtained by ground-based observations.

To obtain reliable $\text{Ly}\alpha$ spatial offsets, we use objects with $I_{814}/H_{160} < 26.5$ and NB387 < 24.5 in this analysis. In this case, 106 and 40 LAEs are selected in I_{814} and H_{160} , respectively. Moreover, no systematic error in the simulation ensures a statistical investigation of the $\text{Ly}\alpha$ spatial offset. NB387 and I_{814} images of example galaxies are shown in Figure 5. We provide the dependence of $\delta_{\text{Ly}\alpha}$ on $\text{Ly}\alpha$ EW in Section 4.2.

3.4. Ellipticity

We measure the ellipticity ϵ of the counterparts in I_{814}/H_{160} using the GALFIT software (Peng et al. 2002, 2010). The ellipticity is defined as $\epsilon = 1 - b/a$, where a and b are the major

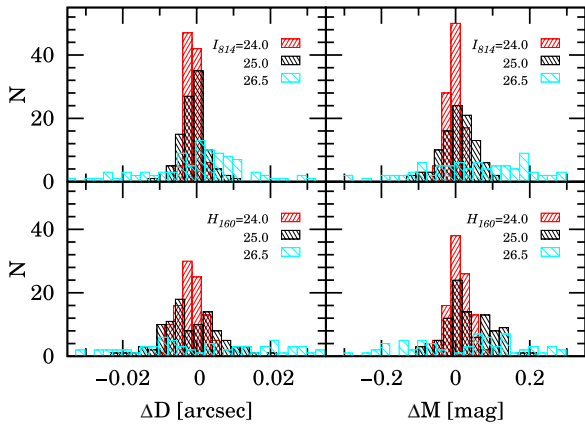


Figure 6. Difference between input and output values of positions (left) and magnitudes (right) in I_{814} (top panels) and H_{160} data (bottom panels) for artificial galaxies. One hundred artificial galaxies are created in each magnitude of I_{814} , H_{160} = 24 (red), 25 (black), and 26.5 (cyan). The histograms are slightly shifted along the x-axis for the sake of clarity.

(A color version of this figure is available in the online journal.)

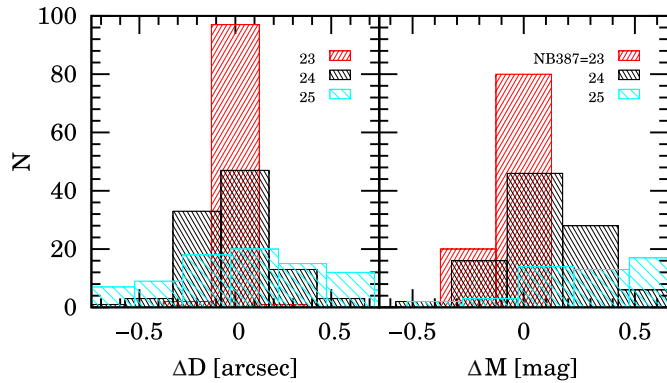


Figure 7. Same as Figure 6, but for Subaru/NB387 images. Artificial galaxies are created in each magnitude of NB387 = 23, 24, and 25.5.

(A color version of this figure is available in the online journal.)

and minor axes, respectively. The ellipticity is calculated for both the brightest and nearest components in the same manner as in Section 3.3. In this calculation, we use objects whose I_{814}/H_{160} magnitudes are brighter than 25.0 and whose half light radii are larger than the typical PSF sizes of each band.

The profile fittings are performed in a manner similar to Gronwall et al. (2011). The counterparts are fitted to a Sérsic profile. Some initial parameters are needed in the GALFIT fitting. The coordinates (x_c , y_c), total magnitude m , axis ratio $q (= b/a)$, position angle, and half light radius r_e of each counterpart are input into the GALFIT configuration file as initial parameters. These initial parameters are estimated with SExtractor prior to the GALFIT fitting. The Sérsic index is set to $n = 4$ (i.e., de Vaucouleurs profile) as an initial value, while the initial Sérsic index does not affect the fitting results (Yuma et al. 2011, 2012). In the fitting procedure, we also allow the following parameters to move in ranges: $24 < m < 29$, $0.1 < r_e < 15$ pixels, $0.1 < n < 15$, $0.1 < q < 1$, $\Delta x < 2$, and $\Delta y < 2$. We create PSF images for I_{814} and H_{160} data by stacking 100 bright isolated point sources. GALFIT outputs best-fit parameters corrected for PSF broadening. Figure 8 shows examples of original I_{814} images, the best-fit Sérsic profiles, and their residual images. As shown in Figure 8, the GALFIT fits the stellar-continuum emission to Sérsic profiles well.

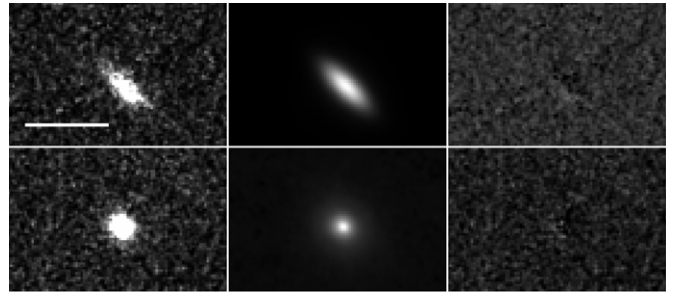


Figure 8. Representative examples with large and small ellipticity in GALFIT fitting. The left, center, and right panels represent I_{814} images, the best-fit Sérsic profiles, and their residual images, respectively. The white bars in the lower corner of each I_{814} image indicates $1''$.

We provide the dependence of ellipticity on $\text{Ly}\alpha$ EW in Section 4.3.

4. RESULTS

In this section, we show the derived merger fraction, $\text{Ly}\alpha$ spatial offset, and ellipticity as a function of $\text{EW}(\text{Ly}\alpha)$. We divide our LAE sample into three $\text{EW}(\text{Ly}\alpha)$ bins, 20–50, 50–100, and $>100 \text{ \AA}$.

4.1. Dependence of Merger Fraction on $\text{Ly}\alpha$ EW

We first compare the merger fractions of the entire sample with results from previous studies for LAEs at $z \sim 2\text{--}6$. The merger fractions in I_{814} and H_{160} are 0.23 ± 0.02 and 0.14 ± 0.02 , respectively, in the close-pair method. These values are broadly consistent with other studies using similar methods (e.g., Taniguchi et al. 2009; Pirzkal et al. 2007; Cowie et al. 2010; Bond et al. 2009). Pirzkal et al. (2007) investigated the rest-frame UV morphologies of nine LAEs at $4 \lesssim z \lesssim 5.7$ based on the C–A classification. They find that $\sim 30\text{--}40\%$ of the sample show clumpy, complex, or morphologically disturbed structures. Taniguchi et al. (2009) determine that only two out of ~ 50 LAEs at $z = 5.7$ have double-component structures, and $\sim 50\%$ of the sample are spatially extended in the rest-frame UV. Bond et al. (2009) determine that at least $\sim 17\%$ of their 120 LAEs at $z = 3.1$ have multiple components. Cowie et al. (2010) claim that $>30\%$ of $z \sim 0.3$ LAEs show merger features. Theoretically, the dark matter simulation combined with the physical model of Tilvi et al. (2011) predicts that the merger fraction of $z \sim 3$ LAEs is ~ 0.20 after matching the merger mass ratio with that of observational studies. Our merger fractions are also nearly the same as those of LBGs at $1.5 \lesssim z \lesssim 3$ estimated with the close-pair method ($\sim 0.05\text{--}0.2$; Law et al. 2012b). Our merger fractions in the A classification are also similar to those of their LBG sample estimated with the same method.

Next, we examine the dependence of the merger fraction on $\text{Ly}\alpha$ EW. Figure 9 shows the derived merger fractions in each $\text{EW}(\text{Ly}\alpha)$ bin. The error bars in each plot include the Poisson statistical errors. We find that the merger fraction does not significantly increase with $\text{Ly}\alpha$ EW in all cases. Instead, merger fractions decrease from the lowest to the highest EW bin over the 1σ error bars in several cases. The merger fractions in H_{160} are a factor of $\sim 2\text{--}3$ lower than those in I_{814} in the corresponding methods. This is likely to be caused by the difference in completeness (Section 3.2.1). In addition to the completeness effect, the difference of the merger fractions could be explained by the shapes of the SEDs, since the

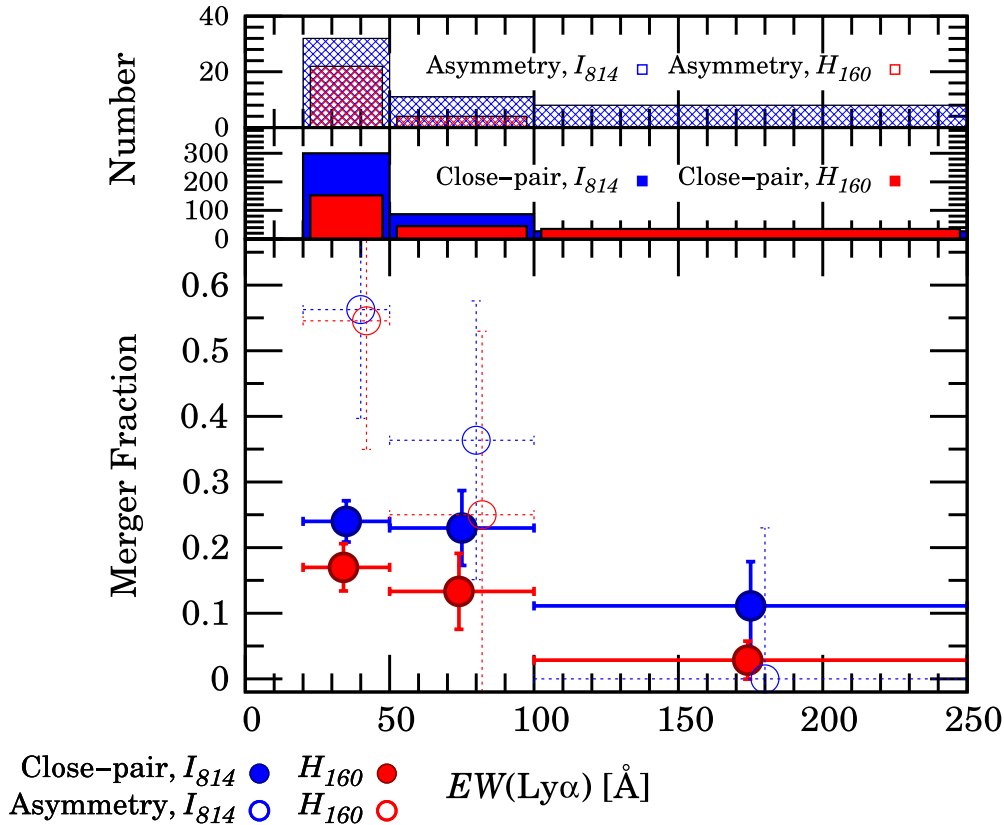


Figure 9. Merger fraction of $z = 2.2$ LAEs as a function of $\text{Ly}\alpha$ EW. The blue and red symbols indicate the merger fractions in I_{814} and H_{160} , respectively. The filled and open circles denote the merger fraction in the close-pair method and the A classification, respectively. Error bars in each plot include the Poisson statistical error. Error bars in $\text{Ly}\alpha$ EW indicate the bin widths. The symbols are slightly shifted along the x-axis for the sake of clarity. There are no LAEs in H_{160} in the highest EW bin for the A classification, because no mergers are found in this EW bin. The histograms in the upper and middle panels show the number of LAEs in each $\text{Ly}\alpha$ EW bin in the A classification and the close-pair method, respectively.

(A color version of this figure is available in the online journal.)

I_{814} - and H_{160} -band data trace the rest-frame UV and optical stellar continuum emission, respectively. We also examine the total merger fraction derived in combination with the close-pair and morphological index methods. We define the total merger fraction as the logical sum of mergers identified by the close-pair method and A classification. However, we do not find the increase of the merger fraction with $\text{EW}(\text{Ly}\alpha)$, similar to Figure 9. We additionally calculate the $\text{Ly}\alpha$ EW from the total magnitudes in the NB data, and evaluate the effect of the $\text{Ly}\alpha$ flux loss in the aperture photometry on the $\text{Ly}\alpha$ dependence. We compute the total magnitudes with MAG_AUTO of SExtractor. Even in this test, we still do not find the trend that the merger fraction increases with $\text{Ly}\alpha$ EW.

We change the selection radius to $r_{\text{sel}} = 1''.5$ (~ 13 kpc at $z = 2.2$) in order to check possible differences in the merger fraction between the searching radii. The $1''.5$ radius is the same as that used in Law et al. (2012b). However, we do not find a significant rise of merger fraction even in the larger radius. The merger fractions with $r_{\text{sel}} = 1''.5$ are a factor of ~ 2 higher than those with $r_{\text{sel}} = 0''.65$. Adopting the $1''.5$ aperture, the merger fractions increase to 0.35 ± 0.03 in I_{814} and 0.30 ± 0.03 in H_{160} . We confirm that the trend of Figure 9 is also found in the results of the $r_{\text{sel}} = 1''.5$ aperture.

The dependence of the merger fraction on the $\text{Ly}\alpha$ EW is also clearly shown in Figure 10. The figure illustrates a trend where objects with a larger $\text{Ly}\alpha$ EW have a smaller half light radius, as claimed by, e.g., Law et al. (2012a) and Pentericci et al. (2010), which is also justified by our statistical tests.

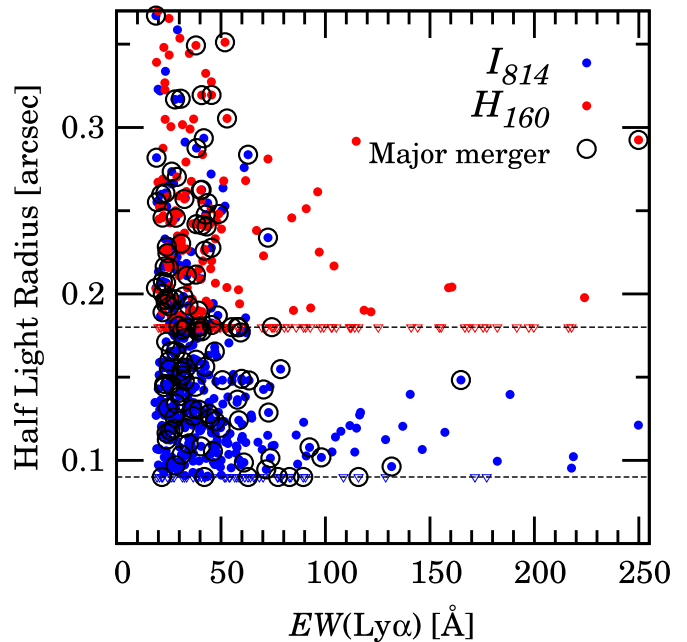


Figure 10. Half light radius and $\text{Ly}\alpha$ EW of continuum counterparts in I_{814} (blue) and H_{160} (red) data. The black open circles mark objects with multiple components in a selection radius of $0''.65$ (major mergers). The horizontal lines indicate typical PSF sizes of I_{814} and H_{160} bands. Objects smaller than the typical PSF sizes are placed at $0''.09$ in I_{814} and $0''.18$ in H_{160} (open inverted triangles).

(A color version of this figure is available in the online journal.)

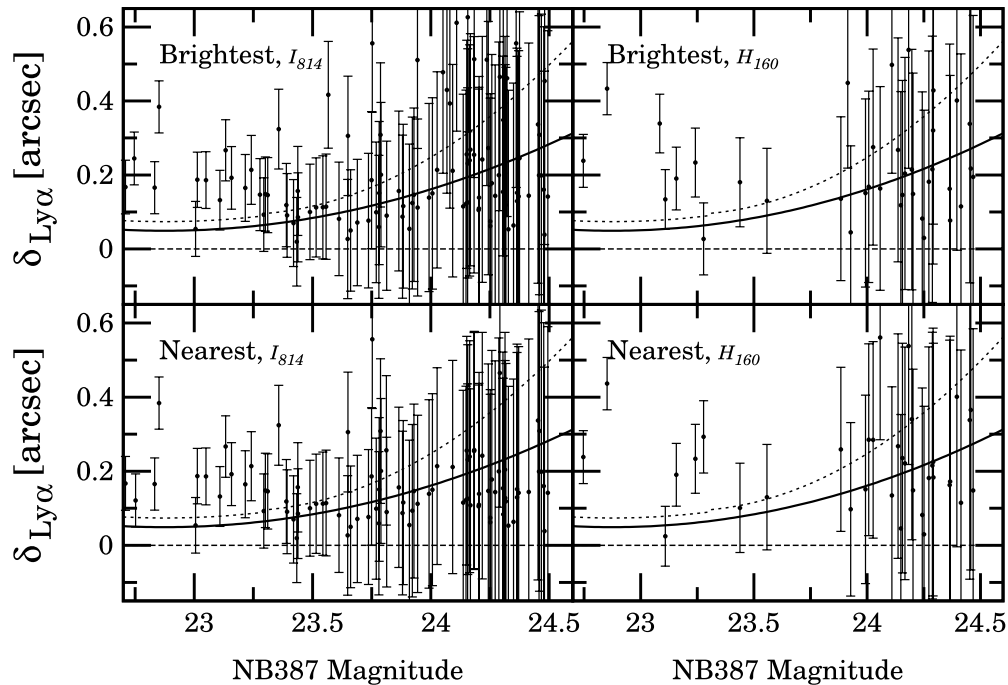


Figure 11. Spatial offset as a function of NB387 magnitude for the brightest counterparts in I_{814} (upper left), and H_{160} (upper right), and the nearest ones in I_{814} (bottom left), and H_{160} (bottom right). The bold and dashed curves denote mean values of $\delta_{\text{Ly}\alpha}$, and their 1σ standard deviations, respectively, estimated from the Monte Carlo simulations in Section 3.2.1. The error bars in $\delta_{\text{Ly}\alpha}$ are based on the positional uncertainties quantified in these simulations.

The individual LAEs identified in the close-pair method are marked by the black circles. Figure 10 clearly exhibits the small number of mergers at $\text{EW}(\text{Ly}\alpha) > 100 \text{ \AA}$. Note that the decline in the merger fraction in high $\text{EW}(\text{Ly}\alpha)$ bins is caused by many incomplete detections of fainter merger components in LAEs with a high EW. Our magnitude cut of 26.5 mag ensures that there is no bias in the I_{814}/H_{160} magnitudes between EW bins (Figure 1). The merger completeness is considered to be almost constant in all of the EW bins.

4.2. Dependence of $\text{Ly}\alpha$ Spatial Offset on $\text{Ly}\alpha$ EW

We investigate the $\delta_{\text{Ly}\alpha}$ of the $\text{Ly}\alpha$ spatial offset and examine whether $\delta_{\text{Ly}\alpha}$ is produced by measurement errors or a real signal. Figure 11 shows $\delta_{\text{Ly}\alpha}$ as a function of NB387 magnitude. We include statistical errors estimated from the Monte Carlo simulation (Section 3.3) in $\delta_{\text{Ly}\alpha}$. We find a tendency that the error in $\delta_{\text{Ly}\alpha}$ becomes larger for the objects with a fainter NB387 magnitude, but successfully identify that several LAEs have an offset beyond our statistical errors for relatively bright objects. The identification of the large $\delta_{\text{Ly}\alpha}$ objects could not be due to large scatters in $\delta_{\text{Ly}\alpha}$, which is justified by our non-parametric Kolmogorov–Smirnov (K-S) tests between the LAEs and artificial galaxies in each NB387 magnitude bin. The K-S probabilities are calculated to be $P_{\text{KS}} \lesssim 0.05$.

Next, we investigate the dependence of $\delta_{\text{Ly}\alpha}$ on $\text{Ly}\alpha$ EW for the brightest continuum sources in Figure 12 and the nearest ones in Figure 13. We find that there are few LAEs with a high EW and a large $\delta_{\text{Ly}\alpha}$. LAEs with a high $\text{Ly}\alpha$ EW tend to have a single continuum counterpart, as described in Section 4.1. The distribution of $\delta_{\text{Ly}\alpha}$ for high EW objects does not depend strongly on whether we use the brightest or the nearest continuum counterparts.

We carry out the K-S test in order to evaluate whether $\delta_{\text{Ly}\alpha}$ is statistically related to $\text{Ly}\alpha$ EW. We calculate the K-S probability that LAEs with $\text{Ly}\alpha$ EW $> 100 \text{ \AA}$ and $< 100 \text{ \AA}$ are drawn from the statistically same distribution of the $\text{Ly}\alpha$ spatial offset. We

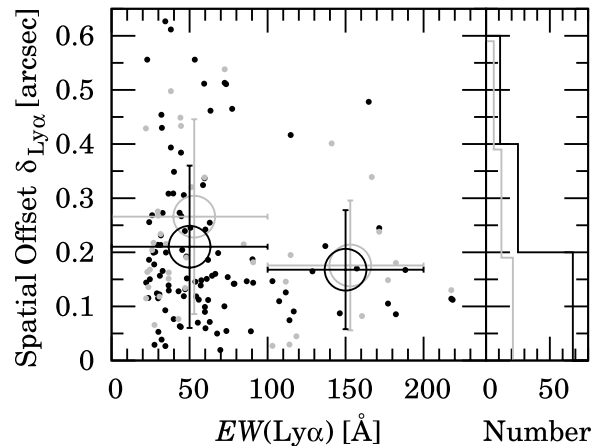


Figure 12. Spatial offset between the rest-frame UV/optical continuum emission of the brightest counterparts and their $\text{Ly}\alpha$ centroids. The black and gray filled circles indicate counterparts in the I_{814} and H_{160} cutout images, respectively. The large black and gray circles are the average values of $\delta_{\text{Ly}\alpha}$ in subsamples of $\text{EW} < 100$, and $> 100 \text{ \AA}$. The right panel shows histograms for the number of LAEs. The histograms are slightly shifted along the y-axis for the sake of clarity. The position of $\text{Ly}\alpha$ emission is redefined in the SExtractor detection with a higher DETECT_THRESH value. Details are described in Section 3.3.

summarize the K-S probabilities, P_{KS} , in Table 3. The P_{KS} values are 0.05–0.1 in the case of the original $\text{Ly}\alpha$ centroid. In the I_{814} data, the low P_{KS} values indicate that the two groups of $\delta_{\text{Ly}\alpha}$ are drawn from statistically different distribution. Even in the case of the redefined values of $\delta_{\text{Ly}\alpha}$, the probabilities are not significantly changed ($P_{\text{KS}} \sim 0.1\text{--}0.3$).

4.3. Dependence of Ellipticity on $\text{Ly}\alpha$ EW

We show the ellipticities of the brightest and nearest continuum objects in Figures 14 and 15, respectively. The average ellipticity of LAEs with $\text{EW}(\text{Ly}\alpha) > 100 \text{ \AA}$ is smaller than that of objects with $\text{EW}(\text{Ly}\alpha) < 100 \text{ \AA}$. There is a possible trend

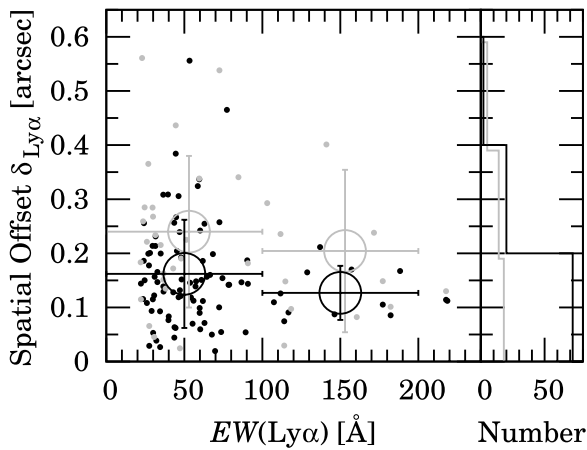


Figure 13. Same as Figure 12, but for the nearest counterparts.

Table 3
Results of Our K-S Test

Quantity (1)	Counterpart and Band (2)	P_{KS} (3)
Ly α spatial offset	Brightest (I_{814})	0.262 (0.096)
	Brightest (H_{160})	0.285 (0.097)
	Nearest (I_{814})	0.177 (0.145)
	Nearest (H_{160})	0.147 (0.050)
Ellipticity	Brightest (I_{814})	0.579
	Brightest (H_{160})	— ^a
	Nearest (I_{814})	0.564
	Nearest (H_{160})	— ^a

Notes. Columns: (1) Quantity. (2) Type of continuum counterparts (*brightest* or *nearest*), and used *HST* band. (3) K-S probability that LAEs with Ly α EW < 100 Å and > 100 Å are drawn from the statistically same distribution. The values in parentheses represent the probabilities for the distribution of $\delta_{Ly\alpha}$ after correcting for the NB centroids with a higher DETECT_THRESH. See Section 3.3.

^a K-S probabilities cannot be calculated because only one object with $EW(Ly\alpha) > 100$ Å matches the selection criteria in the H_{160} data.

that the LAEs with a large Ly α EW have a small ellipticity for both the brightest and nearest components. The right panel of each figure displays histograms of the ellipticity. The ellipticity distribution is quite similar to that estimated by Gronwall et al. (2011), who have studied the morphologies of LAEs at similar redshift.

We calculate the K-S probability for the ellipticity in a similar manner as for the Ly α spatial offset in Section 4.2. The probabilities are listed in Table 3. The probabilities are calculated to be 0.5–0.6 in the I_{814} data. The high values indicate that LAEs with Ly α EW > 100 Å and < 100 Å have statistically indistinguishable distributions. These probabilities suggest that the dependence of ellipticity on Ly α EW cannot be concluded in a statistical sense. The small sample size of LAEs with $EW(Ly\alpha) > 100$ Å may not allow us to obtain accurate K-S probabilities.

5. DISCUSSION

5.1. Ly α Enhancement by Major Merger

In Section 4.1, we find that the merger fraction of LAEs does not significantly increase with their Ly α EW. Instead, Figure 9 shows the merger fraction decreases from $EW(Ly\alpha) = 20$ –100 to > 100 Å. However, our statistical analysis indicates that mergers are rare in the subsample of LAEs with a Ly α EW

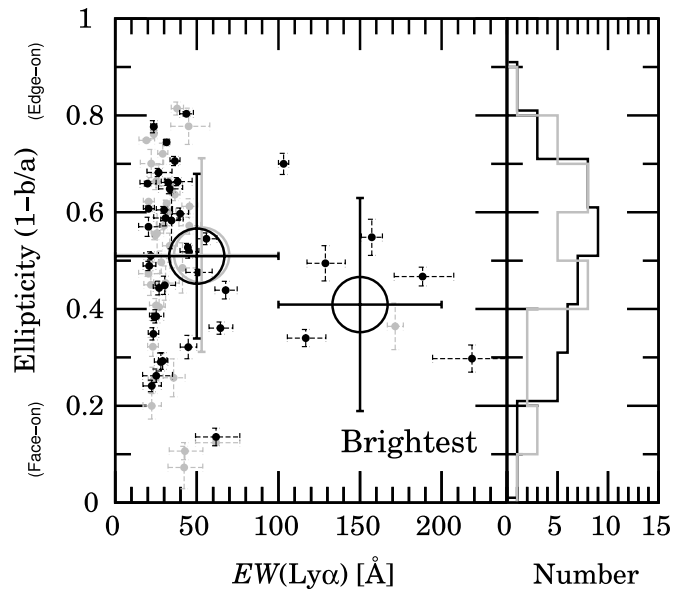


Figure 14. Ellipticity of the brightest continuum counterparts and its dependence on their Ly α EW. The black and gray filled circles indicate counterparts in I_{814} and H_{160} cutout images, respectively. The large black and gray circles are the average ellipticity in subsamples of $EW < 100$ and > 100 Å. The right panel shows histograms for the number of LAEs. The histograms are slightly shifted along the y-axis for the sake of clarity.

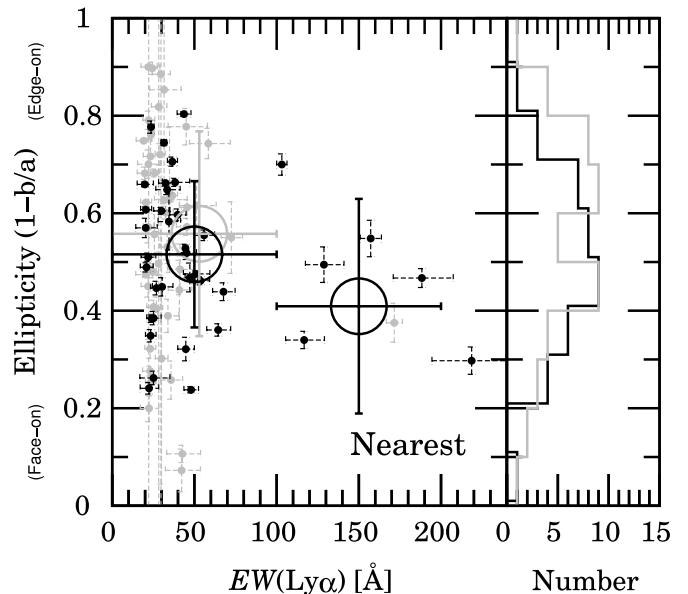


Figure 15. Same as Figure 14, but for the nearest continuum counterparts.

larger than 100 Å. Our result would suggest that the galaxy merger does not heavily affect the distribution of H I gas and dust. On the contrary, the H I clouds disturbed by a merger would envelop a central ionizing source instead of making holes in the gas shell. The nearly uniform clouds might prevent Ly α photons from easily escaping from a galaxy.

This is opposite to the trend where Ly α emission is enhanced by a galaxy merger. Several observational studies have examined a relationship between Ly α EW and galaxy merger in the LAE population. For example, Cooke et al. (2010) and Chonis et al. (2013) claim that Ly α emission is enhanced by galaxy mergers. This trend is commonly based on the idea that a galaxy interaction triggers star formation, and disperses obscuring gas and dust in the system (e.g., Chonis et al. 2013).

Cooke et al. (2010) carry out spectroscopic observations for 140 LBGs at $z \sim 3$ and find serendipitously five LBG pairs with projected proper separations of less than 15 kpc. They additionally discover two LAEs with a close LBG in their MOS slitlets. One of these LAEs has a Ly α EW of 48 Å. The separation between the LAE and its LBG companion is 22.7 kpc. Another LAE has a Ly α EW of 140 Å, but its LBG companion is not definitively confirmed by spectroscopy. This merger candidate has a relatively large projected separation of 40.1 kpc between its components. In this survey, only one object with such a high EW has been found in the seven serendipitously discovered close pairs ($\sim 14\%$) if the LAE with $\text{EW}(\text{Ly}\alpha) = 140$ Å is a genuine merger.

Recently, Chonis et al. (2013) investigated three LAEs in the HETDEX sample. The Ly α EW of all the three LAEs exceeds 100 Å (114 ± 13 , 140 ± 43 , and 206 ± 65 Å) due to a unique LAE selection method of the HETDEX survey (Adams et al. 2011). In the *HST* images, two LAEs with $\text{EW}(\text{Ly}\alpha) = 114$ and 140 Å show close components with projected separations of ~ 5 and 8 kpc, respectively. One of these close components has also been spectroscopically confirmed to be at the same redshift as its central LAE. The LAE with the highest EW of 206 Å does not have a companion within 1'' (~ 8.2 kpc).⁷ Thus, the merger fraction at $\text{EW}(\text{Ly}\alpha) > 100$ Å is $0.67^{+0.33}_{-0.43}$ in their HETDEX sample. The error is due to the small number statistics (Gehrels 1986). Our merger fraction at $\text{EW}(\text{Ly}\alpha) > 100$ is 0.23 ± 0.08 in I_{814} in a searching radius of 1/5 (~ 13 kpc) similar to that of Chonis et al. (2013). The merger fractions are consistent within 1σ uncertainties. In the study of Chonis et al. (2013), the merger fraction at $\text{EW}(\text{Ly}\alpha) > 100$ Å probably becomes higher due to the small number of sample objects.

In contrast to these suggestions, some morphological studies provide results that are consistent with our Ly α dependence. Law et al. (2007) have investigated the morphologies of 216 $z \sim 2$ –3 LBGs with spectroscopic redshifts using the *HST* data. They quantify a multiplicity of a galaxy with the multiplicity parameter Ψ . The value of Ψ is zero for a galaxy with a single component and becomes positive for a galaxy with multiple components. This parameter is used to find multiple components, which is similar to our close-pair method. They reveal that the Ly α EW monotonically increases from 0 to 15 Å with decreasing Ψ . This trend is consistent with the behavior of our merger fractions in the EW range of 20–200 Å, which is larger than the EW range of Law et al. (2007). Pentericci et al. (2010) have measured the asymmetry parameter for $z \sim 3$ LBGs with and without Ly α emission. They find no difference of A between LBGs with a high and a low EW. The decrease in the merger fraction for our LAEs might be found in the wider dynamic range in $\text{EW}(\text{Ly}\alpha)$ than that of their LBG sample.

Another explanation is that dust created by past star-formation in individual pre-mergers produces the anti-correlation between Ly α EW and merger fraction. The star formation triggered by a major merger would enhance Ly α emission, but Ly α photons could be absorbed by the dust already existing in individual evolved galaxies. For this reason, Ly α EW would be less enhanced in a system consisting of evolved major merger components, which would yield the anti-correlation.

In addition to observational studies, Yajima et al. (2013) have investigated the physical properties of interacting Ly α Blob (LAB) pairs by combining hydrodynamical simulations with three-dimensional radiative transfer calculations. The star

formation rate (SFR) of LABs is boosted during each galaxy-coalescence phase. In contrast to SFR, Ly α EW fluctuates in the range of 20–100 Å, and is not enhanced to > 100 Å even at the time of coalescences. Note that the simulated LABs have a larger size and slightly brighter Ly α luminosity than those of our normal LAEs.

There is a possibility that the anti-correlation between the merger fraction and Ly α EW could be produced by a difference of viewing angle. In this study, we have defined mergers as objects with multi-components or interacting features shown in the plane of the sky. However, mergers along the line of sight would boost the radial velocity of the surrounding gas clouds, and consequently enhance the Ly α escape in the direction of the observer. The detection of the line-of-sight mergers could be more challenging than the identification of interacting events shown in the plane of the sky.

5.2. Where Is Ly α Emitted From?

We find that there are few LAEs with a high Ly α EW and a large $\delta_{\text{Ly}\alpha}$. The dependence of $\delta_{\text{Ly}\alpha}$ on Ly α EW would suggest that Ly α photons could be heavily attenuated by dust on the long path lengths prior to escaping an H I cloud. This might yield a $\delta_{\text{Ly}\alpha}$ difference in objects with a high and a low Ly α EW.

Prior to our statistical study, several NB imaging studies have also estimated $\delta_{\text{Ly}\alpha}$ for high- z LAEs. Jiang et al. (2013) have studied rest-frame UV morphologies of 51 LAEs at $z \sim 5.7, 6.5$, and 7.0 using the *HST* data. The Ly α positions of these LAEs have been estimated in NB images taken with Subaru/Suprime-Cam. They find that several LAEs show evidence of positional offset between UV and Ly α emission. In these $z \sim 6$ –7 LAE samples, LAEs with a spatially symmetric light profile tend to have a small $\delta_{\text{Ly}\alpha}$. The offset is also shown in an extended Ly α emission, Himiko, at $z = 6.595$ (Ouchi et al. 2013). Rauch et al. (2011) find a large positional offset in a galaxy at $z = 3.334$ based on a deep spectroscopic survey. For the $z = 3.334$ galaxy, the Ly α and UV structure is highly peculiar and is likely to be affected by several physical processes, such as cold gas inflow.

In contrast, most of these LAEs with a large $\delta_{\text{Ly}\alpha}$ show merger and/or interacting features. Finkelstein et al. (2011) have performed high resolution imaging observations with an NB filter on *HST* for three LAEs at $z = 4.4$. They do not find positional offsets between resolved Ly α and UV continuum emission. All three LAEs observed with *HST* also show no evidence of major merger/galaxy interactions.

These results would indicate that the relatively small $\delta_{\text{Ly}\alpha}$ in high EW objects originates from physically stable and spatially symmetric H I gas clouds around a central ionizing source(s). On the contrary, the large $\delta_{\text{Ly}\alpha}$ could result from inhomogeneous H I gas clouds disturbed by a merger. The disturbed clouds prevent Ly α radiation from escaping directly along the line of sight, making a large $\delta_{\text{Ly}\alpha}$ from an original position of the stellar component. A large number for resonant scattering would suppress Ly α EW on the long path lengths in the disturbed clouds.

5.3. Galactic Inclination Effect on Ly α Emissivity

We find that there is a trend where the LAEs with a large Ly α EW have a small ellipticity. Figures 14 and 15 show a possible absence of objects at a high ellipticity and Ly α EW region (in the upper right corner in the figures). This trend is consistent with the recent theoretical claims that Ly α photons can more easily escape from face-on disks having a small ellipticity due

⁷ A nearby continuum source is shown at a projected distance of 4'' (~ 33 kpc) from the LAE.

to a low H I column density (e.g., Verhamme et al. 2012; Yajima et al. 2012b).

The ellipticity is a useful indicator of the galactic disk inclination. Verhamme et al. (2012) have investigated quantitatively the effect using their Ly α radiative transfer code combined with hydrodynamics simulations. They find that the Ly α EW strongly depends on the inclination for a simulated galaxy with thick star-forming clouds. From edge-on to face-on, the Ly α EW increases from -5 to 90 Å. Yajima et al. (2012b) have predicted that the Ly α flux is 100 times brighter in the face-on direction than the edge-on.

However, our K-S test does not definitively indicate that there is an anti-correlation between Ly α EW and the ellipticity (Section 4.3). The sample size of our high EW LAEs may be too small to obtain conclusive evidence of the anti-correlation. We require a larger LAE sample containing many high EW (>100 Å) objects bright ($m_{\text{cont}} < 25$) enough to measure robustly their morphologies.

5.4. What is the Physical Origin of Strong Ly α Emission?

Our results for Ly α EW dependence generally support the idea that an H I column density is a key quantity determining Ly α emissivity. We find that LAEs with $\text{EW}(\text{Ly}\alpha) > 100$ Å tend to be a non-merger (Section 4.1) and compact (Figure 10), and to have a small ellipticity (Section 4.3) in our structure analyses. Our magnitude cut allows us to fairly compare structural properties between each $\text{EW}(\text{Ly}\alpha)$ bin under the same ranges of galaxy-luminosity-correlating mass (Figure 1). We also verify the above trends by using objects with a similar size, but we do not find any significant changes. These results could attribute the $\text{EW}(\text{Ly}\alpha)$ dependences on the LAE structures to predominantly Ly α emissivity rather than the galaxy mass. These trends do not depend strongly on whether we use the brightest or nearest counterparts.

Recent spectroscopic studies measure the Ly α velocity offset, $\Delta v_{\text{Ly}\alpha}$, from the systemic redshift estimated from nebular lines for a number of LAEs (Hashimoto et al. 2013; Shibuya et al. 2014). Their kinematic analyses have suggested that LAEs typically have a smaller $\Delta v_{\text{Ly}\alpha}$ than that of LBGs with a lower Ly α EW, while their outflowing velocities are similar in the two populations. This indicates that the small $\Delta v_{\text{Ly}\alpha}$ of LAEs is caused by a low H I column density. On the other hand, NIR spectroscopy by Nakajima et al. (2013) has suggested that LAEs have a large $[\text{O III}]/[\text{O II}]$ ratio, indicating that these systems are highly ionized with density-bounded H II regions. This tendency has been confirmed by a subsequent systematic study in Nakajima & Ouchi (2013). The large $[\text{O III}]/[\text{O II}]$ ratio also indicates a low column density of H I gas. Based on these results for the gas distribution and abundances, the difference in H I column density simply explains the Ly α -EW dependences of the merger fraction, the Ly α spatial offset, and the galaxy inclination. For objects with density-bounded H II regions, Ly α photons would directly escape from central ionizing sources which produce a small $\delta_{\text{Ly}\alpha}$. The low H I abundance along the line of sight also induces the preferential escape of Ly α to the face-on direction. For these reasons, ionized regions with small amounts of H I gas would dominate in the subsample of our LAEs with $\text{EW} > 100$ Å.

6. SUMMARY AND CONCLUSION

We examine the structural properties of LAEs at $z = 2.2$ using the *HST* high resolution images in order to investigate the

Ly α emitting mechanisms. By using the large LAE sample of 426 objects, we study statistically the Ly α -EW dependence on the merger fraction, the Ly α spatial offset, $\delta_{\text{Ly}\alpha}$, and ellipticity for the first time.

The conclusions of our structure analyses for LAEs are summarized below.

1. Our results for the merger fraction and the ellipticity distribution are consistent with those in previous morphological studies for LAEs at various redshifts. The merger fraction and the average ellipticity of a LAE's stellar component are 10%–30% and 0.4–0.6, respectively.
2. The merger fractions of LAEs do not significantly increase with their Ly α EW. This trend is opposite to the physical picture in which the Ly α EW is boosted by the galaxy merger and interaction. H I clouds disturbed by merger would envelop a central ionizing source instead of making holes in the gas clouds. The disturbed clouds may not allow Ly α photons to escape easily from a galaxy.
3. We successfully identify that some LAEs have a spatial offset between Ly α and stellar-continuum emission peaks by $\sim 0''.3$ – $0''.5$ (~ 2.5 – 4 kpc) beyond our statistical errors. We reveal an anti-correlation between $\delta_{\text{Ly}\alpha}$ and $\text{EW}(\text{Ly}\alpha)$ by a K-S test with two subsamples of $\text{EW}(\text{Ly}\alpha) = 20$ – 100 and >100 Å. The anti-correlation would suggest that Ly α photons could be heavily attenuated by dust on the long path lengths prior to escaping H I clouds. On the contrary, a large $\delta_{\text{Ly}\alpha}$ would result from inhomogeneous H I gas clouds disturbed by merger. The disturbed clouds prevent Ly α radiation from escaping directly along a line of sight, giving a large $\delta_{\text{Ly}\alpha}$. Resonant scattering of long path lengths would suppress Ly α EW in the disturbed clouds.
4. We find that there is a trend that LAEs with a large Ly α EW have a small ellipticity. This is consistent with the recent theoretical claims that Ly α photons can more easily escape from face-on disks having a small ellipticity, due to a low H I column density, although our K-S test indicates that this trend is not significant in a statistical sense. However, this K-S test result might originate from the small number of bright and spatially resolved objects with a high EW whose morphological properties are estimated robustly.
5. Our results of Ly α -EW dependence generally support the idea that an H I column density is a key quantity determining Ly α emissivity. In this condition, Ly α photons would directly escape from central ionizing sources. The difference in H I abundance along the line of sight is expected to yield naturally the Ly α -EW dependences of the merger fraction, the Ly α spatial offset, and the galaxy inclination.

An upcoming extensive survey for LAEs at $z = 2$ – 7 with Hyper Suprime-Cam (HSC) on Subaru will identify a large number of unique high EW objects whose number is not high enough in our study. Future HSC studies will test the possible anti-correlation between Ly α EW and ellipticity with large statistical samples.

We thank Anne Verhamme, Zheng Zheng, Michael Rauch, Lucia Guaita, and Akio Inoue for useful discussion, and an anonymous referee for constructive comments. This work is based on observations taken by the CANDELS Multi-Cycle Treasury Program with the NASA/ESA *HST*, which is operated by the Association of Universities for Research in Astronomy, Inc., under NASA contract NAS5-26555. The NB387 data

used in this work were collected at the Subaru Telescope, which is operated by the National Astronomical Observatory of Japan. This work is based in part on observations made with the Spitzer Space Telescope, which is operated by the Jet Propulsion Laboratory, California Institute of Technology under a contract with NASA. Support for this work was provided by NASA through an award issued by JPL/Caltech. This work was supported by World Premier International Research Center Initiative (WPI Initiative), MEXT, Japan. This work was supported by KAKENHI (23244025) and (21244013) Grant-in-Aid for Scientific Research (A) through Japan Society for the Promotion of Science (JSPS).

Facilities: Subaru (Suprime-Cam), HST/ACS, WFC3

REFERENCES

- Abraham, R. G., van den Bergh, S., Glazebrook, K., et al. 1996, *ApJS*, **107**, 1
- Adams, J. J., Blanc, G. A., Hill, G. J., et al. 2011, *ApJS*, **192**, 5
- Ando, M., Ohta, K., Iwata, I., et al. 2006, *ApJL*, **645**, L9
- Barnes, L. A., Haehnelt, M. G., Tescari, E., & Viel, M. 2011, *MNRAS*, **416**, 1723
- Bertin, E., & Arnouts, S. 1996, *A&AS*, **117**, 393
- Bond, N. A., Feldmeier, J. J., Matković, A., et al. 2010, *ApJL*, **716**, L200
- Bond, N. A., Gawiser, E., Gronwall, C., et al. 2009, *ApJ*, **705**, 639
- Bond, N. A., Gawiser, E., Guaita, L., et al. 2012, *ApJ*, **753**, 95
- Cassata, P., Guzzo, L., Franceschini, A., et al. 2007, *ApJS*, **172**, 270
- Charlot, S., & Fall, S. M. 1993, *ApJ*, **415**, 580
- Chen, W. L., & Neufeld, D. A. 1994, *ApJ*, **432**, 567
- Chonis, T. S., Blanc, G. A., Hill, G. J., et al. 2013, *ApJ*, **775**, 99
- Ciardullo, R., Gronwall, C., Wolf, C., et al. 2012, *ApJ*, **744**, 110
- Conselice, C. J. 2003, *ApJS*, **147**, 1
- Conselice, C. J., & Arnold, J. 2009, *MNRAS*, **397**, 208
- Conselice, C. J., Bershad, M. A., & Jangren, A. 2000, *ApJ*, **529**, 886
- Cooke, J., Berrier, J. C., Barton, E. J., Bullock, J. S., & Wolfe, A. M. 2010, *MNRAS*, **403**, 1020
- Cowie, L. L., Barger, A. J., & Hu, E. M. 2010, *ApJ*, **711**, 928
- Dressler, A., Martin, C. L., Henry, A., Sawicki, M., & McCarthy, P. 2011, *ApJ*, **740**, 71
- Duval, F., Schaerer, D., Östlin, G., & Laursen, P. 2014, *A&A*, **562**, 52
- Ellison, S. L., Mendel, J. T., Patton, D. R., & Scudder, J. M. 2013, *MNRAS*, **435**, 3627
- Finkelstein, S. L., Cohen, S. H., Windhorst, R. A., et al. 2011, *ApJ*, **735**, 5
- Finkelstein, S. L., Rhoads, J. E., Malhotra, S., Pirzkal, N., & Wang, J. 2007, *ApJ*, **660**, 1023
- Furusawa, H., Kosugi, G., Akiyama, M., et al. 2008, *ApJS*, **176**, 1
- Gawiser, E., Francke, H., Lai, K., et al. 2007, *ApJ*, **671**, 278
- Gehrels, N. 1986, *ApJ*, **303**, 336
- Giacconi, R., Rosati, P., Tozzi, P., et al. 2001, *ApJ*, **551**, 624
- Gialalisco, M., Ferguson, H. C., Koekemoer, A. M., et al. 2004, *ApJL*, **600**, L93
- Grogin, N. A., Kocevski, D. D., Faber, S. M., et al. 2011, *ApJS*, **197**, 35
- Gronwall, C., Bond, N. A., Ciardullo, R., et al. 2011, *ApJ*, **743**, 9
- Gronwall, C., Ciardullo, R., Hickey, T., et al. 2007, *ApJ*, **667**, 79
- Guaita, L., Acquaviva, V., Padilla, N., et al. 2011, *ApJ*, **733**, 114
- Hashimoto, T., Ouchi, M., Shimasaku, K., et al. 2013, *ApJ*, **765**, 70
- Hu, E. M., Cowie, L. L., Barger, A. J., et al. 2010, *ApJ*, **725**, 394
- Jiang, L., Egami, E., Fan, X., et al. 2013, *ApJ*, **773**, 153
- Kashikawa, N., Shimasaku, K., Malkan, M. A., et al. 2006, *ApJ*, **648**, 7
- Kashikawa, N., Shimasaku, K., Matsuda, Y., et al. 2011, *ApJ*, **734**, 119
- Koekemoer, A. M., Aussel, H., Calzetti, D., et al. 2007, *ApJS*, **172**, 196
- Koekemoer, A. M., Faber, S. M., Ferguson, H. C., et al. 2011, *ApJS*, **197**, 36
- Komatsu, E., Smith, K. M., Dunkley, J., et al. 2011, *ApJS*, **192**, 18
- Laursen, P., Duval, F., & Östlin, G. 2013, *ApJ*, **766**, 124
- Laursen, P., & Sommer-Larsen, J. 2007, *ApJL*, **657**, L69
- Laursen, P., Sommer-Larsen, J., & Andersen, A. C. 2009, *ApJ*, **704**, 1640
- Law, D. R., Steidel, C. C., Erb, D. K., et al. 2007, *ApJ*, **656**, 1
- Law, D. R., Steidel, C. C., Shapley, A. E., et al. 2012a, *ApJ*, **759**, 29
- Law, D. R., Steidel, C. C., Shapley, A. E., et al. 2012b, *ApJ*, **745**, 85
- Le Fèvre, O., Abraham, R., Lilly, S. J., et al. 2000, *MNRAS*, **311**, 565
- Lotz, J. M., Jonsson, P., Cox, T. J., & Primack, J. R. 2008, *MNRAS*, **391**, 1137
- Lotz, J. M., Primack, J., & Madau, P. 2004, *AJ*, **128**, 163
- Massey, R., Stoughton, C., Leauthaud, A., et al. 2010, *MNRAS*, **401**, 371
- Miyazaki, S., Komiyama, Y., Sekiguchi, M., et al. 2002, *PASJ*, **54**, 833
- Nakajima, K., & Ouchi, M. 2013, arXiv:1309.0207
- Nakajima, K., Ouchi, M., Shimasaku, K., et al. 2012, *ApJ*, **745**, 12
- Nakajima, K., Ouchi, M., Shimasaku, K., et al. 2013, *ApJ*, **769**, 3
- Oke, J. B., & Gunn, J. E. 1983, *ApJ*, **266**, 713
- Ono, Y., Ouchi, M., Shimasaku, K., et al. 2010, *MNRAS*, **402**, 1580
- Ota, K., Iye, M., Kashikawa, N., et al. 2008, *ApJ*, **677**, 12
- Ouchi, M., Ellis, R., Ono, Y., et al. 2013, *ApJ*, **778**, 102
- Ouchi, M., Shimasaku, K., Akiyama, M., et al. 2008, *ApJS*, **176**, 301
- Ouchi, M., Shimasaku, K., Furusawa, H., et al. 2010, *ApJ*, **723**, 869
- Peng, C. Y., Ho, L. C., Impey, C. D., & Rix, H.-W. 2002, *AJ*, **124**, 266
- Peng, C. Y., Ho, L. C., Impey, C. D., & Rix, H.-W. 2010, *AJ*, **139**, 2097
- Pentericci, L., Grazian, A., Scarlata, C., et al. 2010, *A&A*, **514**, A64
- Petrosian, V. 1976, *ApJL*, **209**, L1
- Pirzkal, N., Malhotra, S., Rhoads, J. E., & Xu, C. 2007, *ApJ*, **667**, 49
- Rauch, M., Becker, G. D., Haehnelt, M. G., et al. 2011, *MNRAS*, **418**, 1115
- Rauch, M., Haehnelt, M., Bunker, A., et al. 2008, *ApJ*, **681**, 856
- Scarlata, C., Carollo, C. M., Lilly, S., et al. 2007, *ApJS*, **172**, 406
- Scoville, N., Aussel, H., Brusa, M., et al. 2007, *ApJS*, **172**, 1
- Shibuya, T., Kashikawa, N., Ota, K., et al. 2012, *ApJ*, **752**, 114
- Shibuya, T., Ouchi, M., Nakajima, K., et al. 2014, arXiv:1402.1168
- Steidel, C. C., Adelberger, K. L., Shapley, A. E., et al. 2000, *ApJ*, **532**, 170
- Taniguchi, Y., Murayama, T., Scoville, N. Z., et al. 2009, *ApJ*, **701**, 915
- Tilvi, V., Scannapieco, E., Malhotra, S., & Rhoads, J. E. 2011, *MNRAS*, **418**, 2196
- Verhamme, A., Dubois, Y., Blaizot, J., et al. 2012, *A&A*, **546**, A111
- Yajima, H., Li, Y., & Zhu, Q. 2013, *ApJ*, **773**, 151
- Yajima, H., Li, Y., Zhu, Q., et al. 2012a, arXiv:1209.5842
- Yajima, H., Li, Y., Zhu, Q., et al. 2012b, *ApJ*, **754**, 118
- Yuma, S., Ohta, K., & Yabe, K. 2012, *ApJ*, **761**, 19
- Yuma, S., Ohta, K., Yabe, K., Kajisawa, M., & Ichikawa, T. 2011, *ApJ*, **736**, 92
- Zamojski, M. A., Schiminovich, D., Rich, R. M., et al. 2007, *ApJS*, **172**, 468
- Zheng, Z., Cen, R., Trac, H., & Miralda-Escudé, J. 2010, *ApJ*, **716**, 574
- Zheng, Z., & Wallace, J. 2013, arXiv:1308.1405